**Article**

# A homogeneous cobalt complex mediated electro and photocatalytic $O_2/H_2O$ interconversion in neutral water



ORR

OER

$O_2$

$H_2O$

$H_2O$   $H_2O_2$   $O_2$

*Bidirectional Catalysis*

Abhishek Saini, Chandan Das, Surabhi Rai, Aritra Guha, Dependu Dolui, Piyali Majumder, Arnab Dutta

arnab.dutta@iitb.ac.in

Highlights

A functional model of $O_2$ carrying metalloproteins

Active for electrocatalytic and photocatalytic ORR and OER in neutral water

Operational for two-electron $O_2/H_2O_2$ four-electron $O_2/H_2O$ reduction pathways

Influential role of flexible ligand environment on ORR and OER catalysis
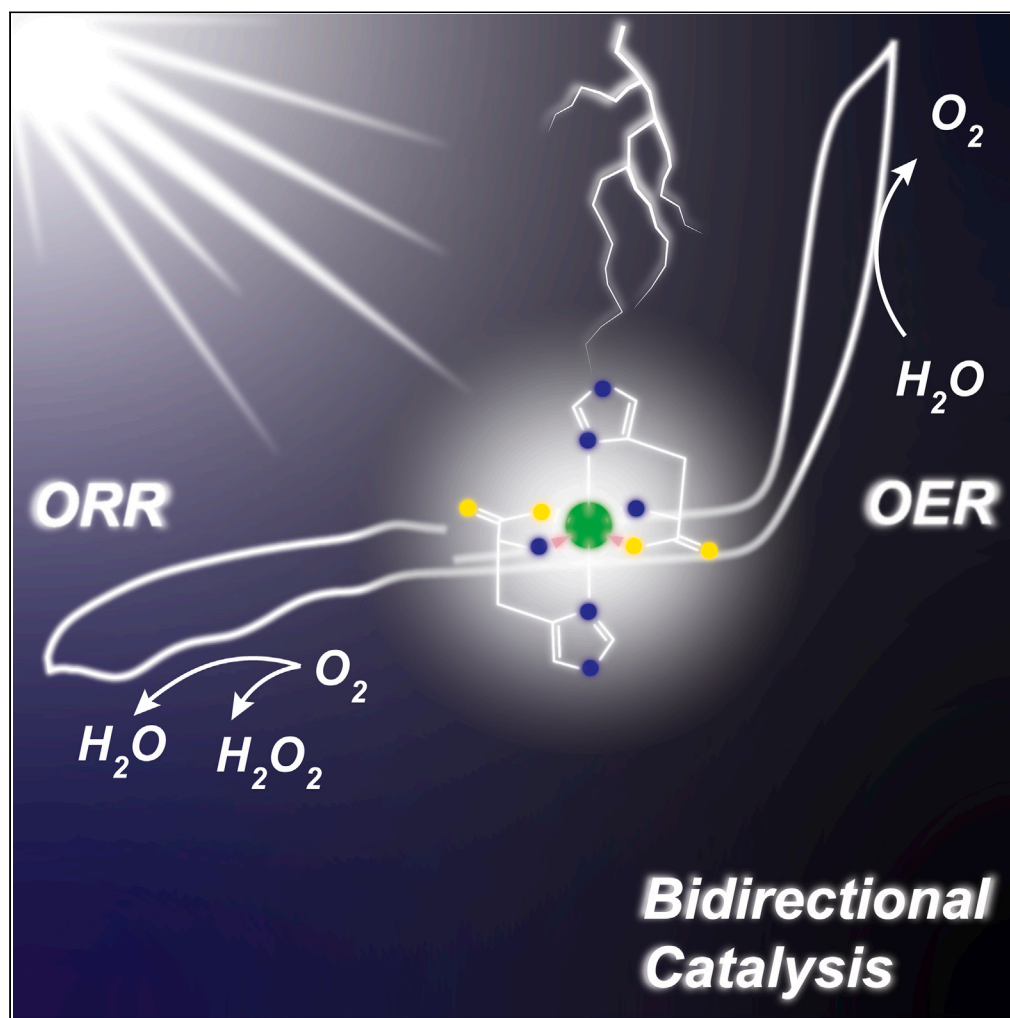
Article

# A homogeneous cobalt complex mediated electro and photocatalytic $O_2/H_2O$ interconversion in neutral water

Abhishek Saini,[1] Chandan Das,[1] Surabhi Rai,[1,3] Aritra Guha,[1] Dependu Dolui,[1] Piyali Majumder,[1] and Arnab Dutta[1,2,3,4,*]

## SUMMARY

**The $O_2/H_2O$ redox couple is vital in various renewable energy conversion strategies. This work delves into the Co(L-histidine)$_2$ complex, a functional mimic of oxygen-carrying metalloproteins, and its electrochemical behavior driving the bidirectional oxygen reduction (ORR) and oxygen evolution (OER) activity in neutral water. This complex electrocatalyzes $O_2$ via two distinct pathways: a two-electron $O_2/H_2O_2$ reduction (catalytic rate = 250 s$^{-1}$) and a four-electron $O_2$ to $H_2O$ production (catalytic rate = 66 s$^{-1}$). The formation of the key trans-μ-1,2-Co(III)-peroxo intermediate expedites this process. Additionally, this complex effectively oxidizes water to $O_2$ (catalytic rate = 15606 s$^{-1}$) at anodic potentials via a Co(IV)-oxo species. Additionally, this complex executes the ORR and OER under photocatalytic conditions in neutral water in the presence of appropriate photosensitizer (Eosin-Y) and redox mediators (triethanolamine/ORR and Na$_2$S$_2$O$_8$/OER) at an appreciable rate. These results highlight one of the early examples of both electro- and photoactive bidirectional ORR/OER catalysts operational in neutral water.**

## INTRODUCTION

The application of small molecule activation reactions for transducing renewable energy resources into readily usable forms has been bolstered by the current interest in sustainable and eco-friendly power generation.[1,2] Here, the conversion between two distinct redox states of a small molecule ensures facile energy mediation via specific chemical bonds.[3] Among multiple accessible options, $O_2/H_2O$ transformation has emerged as one of the leading choices due to the natural abundance of water and oxygen.[4] In this regard, the chemically opposite reactions of oxygen reduction and oxygen evolution from water become critical.[5] Thus, the research community searches for suitable catalysts for supporting both oxygen reduction reaction (ORR) and oxygen evolution reaction (OER), preferably operational under ambient natural conditions.[6,7] The metal-air batteries (MAB) and unitized regenerative fuel cell (URFC) setup require the application of both ORR and OER catalysts to operate in their respective charging/discharging and electrolyzer/fuel cell modes.[8–13] Hence, the generation of bidirectional OER/ORR electrocatalysts is reckoned as a pivotal step for small molecule redox-cycle-based renewable energy conversion.[14–21] The functional modeling of the natural metalloenzymes has emerged as one of the popular choices for replicating the catalytic properties with synthetic model complexes.[22] The natural metalloenzymes hint at the potential infrastructure of catalysts based on inexpensive and readily available first-row transition elements.[23] The Mn$_4$Ca inorganic core of oxygen-evolving complex (OEC) present in the photosystem II (PS II) catalyzes the WOR,[24,25] which has sparked the development of a plethora of artificial molecular OER catalysts.[26–31] Cobalt-based complexes have appeared as a viable option for OEC core replication due to their functional similarity.[32–34] Thus, the development of catalysts with Co$_4$O$_4$ cubanes and derivatives has received appreciable attention.[35–37] Furthermore, the in-depth functional analysis of these catalysts unveiled the involvement of high-valent metal oxo intermediates.[38,39] Despite their impressive OER activities, these catalysts fail to showcase appreciable ORR activities. The same trend continues even with traditional ligand templates where iron-porphyrin complexes[40,41] and cobalt-based complexes[28,42–45] display either ORR or OER activity in water. The inclusion of a dynamic ligand environment is considered to be a key factor in instigating bidirectional catalysis by accommodating the dynamic coordination geometries and variable metal oxidation states. Following this strategy, Dey and co-workers developed Mn-porphyrin complexes for active bidirectional ORR/OER catalysis in both directions in an aqueous solution.[46] Lei and co-workers developed cobalt-corrole complexes to get the same kind of catalytic behavior.[47] However, these catalysts become operational only after their surface immobilization. Very recently, Dutta and co-workers designed a hemilabile ligand scaffold to generate a Cu-N$_4$-core, which displays remarkable bidirectional ORR/OER activity in an aqueous solution.[48] This was one of the first

[1]Chemistry Department, Indian Institute of Technology Bombay, Powai, Mumbai 400076, India
[2]Interdisciplinary Program in Climate Studies, Indian Institute of Technology Bombay, Powai, Mumbai 400076, India
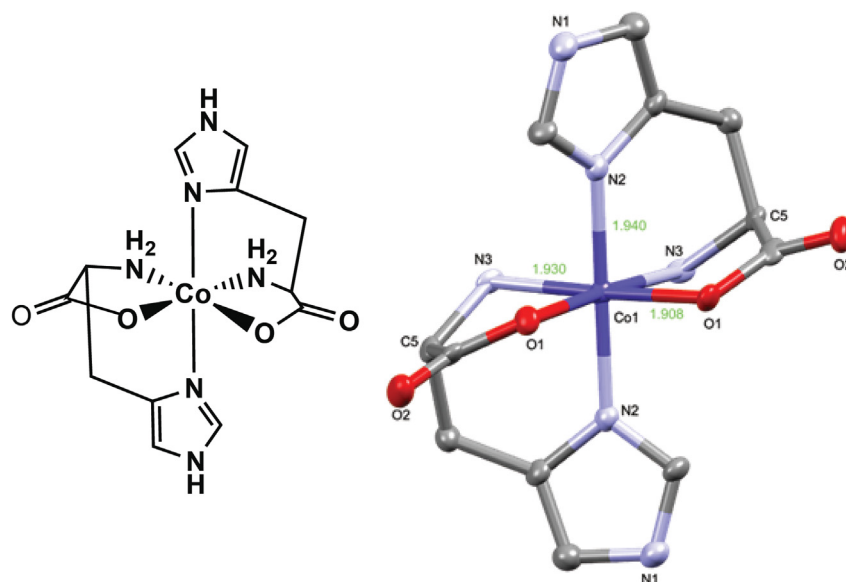[3]National Center of Excellence in CCU, Indian Institute of Technology Bombay, Powai, Mumbai 400076, India
[4]Lead contact
*Correspondence: arnab.dutta@iitb.ac.in
https://doi.org/10.1016/j.isci.2023.108189

**Figure 1. The chemical structure**

The molecular structure of Deoxy-M present in the unit cell with appropriate atom labeling [Co (blue), C (gray), N (sky blue), Oxygen (Red)]. Hydrogen atoms are omitted for clarity. Displacement ellipsoids for non-hydrogen atoms are drawn at 50% probability level.

examples of homogeneous bidirectional $O_2$ reduction/$O_2$ evolution electrocatalysis. Therefore, constructing a homogeneous bidirectional active ORR/OER molecular electrocatalyst still remains in its early stages.

Here, in this study, we have attempted to model the reversible $O_2$-binding metalloproteins for creating a new genre of bidirectional ORR/OER electrocatalysts. The majority of the natural oxygen carrier proteins (hemoglobin, hemerythrin, hemocyanin) exist in two distinct forms: $O_2$-bound oxy and $O_2$-less deoxy, which exhibit distinct spectroscopic signatures. This feature was aptly replicated with a relatively simple cobalt-histidine complex [Co(*L*-His)$_2$] in a neutral aqueous solution.[49,50] The deoxy and oxy versions of this complex were probed in detail by our group recently, where we discovered a redox shuttling between molecular oxygen and peroxide intermediate.[51] This change was aided by a change in the molecularity and oxidation state of the cobalt center as follows: Deoxy complex (mononuclear, Co(II)) and Oxy complex (Dinuclear, Co(III)). The spontaneous stoichiometric conversion of Deoxy to Oxy state following $O_2$ exposure led us to probe the [Co(*L*-His)$_2$] further for possible electrocatalytic ORR activity. Our studies have displayed a two-stage electrocatalytic oxygen reduction by the cobalt complex at pH 7.0. A series of spectroscopic and electrochemical studies indicated the occurrence of $O_2$ to $H_2O_2$ reduction in the first step (catalytic rate = 250 s$^{-1}$, overpotential 0.6 V), whereas the application of further cathodic potential enables a full four-electron reduction of $O_2$ to water (catalytic rate = 66 s$^{-1}$, overpotential 1.55 V). Interestingly, this complex was also found to be active for water oxidation in the identical neutral aqueous media as it produces $O_2$ during the anodic scan (catalytic rate = 15606 s$^{-1}$, overpotential = 0.29 V). The existence of *trans*-μ-1,2-Co(III)-peroxo and Co(IV)-oxo species, which are the key intermediates for ORR and OER pathways, respectively, were identified during the electrocatalytic experiments via spectroelectrochemical experiments. We were also able to unlock the photocatalytic activity of this complex in the presence of Eosin-Y photosensitizer and appropriate redox mediator (triethanolamine/TEOA during ORR and Na$_2$S$_2$O$_8$ during OER). The [Co(*L*-His)$_2$] complex displayed appreciable photocatalytic ORR (TON 249) and OER (TON 540) in a neutral aqueous solution. Such a dual-active and bidirectional OER/ORR catalysis has rarely been achieved in neutral water. Hence, this study sets up a unique template for designing multi-functional catalysts with rational incorporation of earth-abundant transition metals into natural amino-acid-based ligand frameworks for variable energy-relevant applications.

## RESULTS AND DISCUSSION

Recently, we have colorimetrically probed the reversible $O_2$-binding metalloproteins with a synthetic Co(*L*-His)$_2$ complex (M). This complex equilibrates between spectroscopically distinct deoxy- (Deoxy-M) and oxygen-bound (Oxy-M) species in a neutral aqueous solution. This feature was utilized for measuring a wide-range $O_2$ concentration (0%–100%) determination.[51] The Deoxy-M complex was synthesized via the addition of two equivalents of *L*-histidine into an aqueous solution (pH 7.0) of Co(II) under anaerobic conditions (Figure S1). Single crystals of Deoxy-M were obtained following the slow evaporation of a methanol/diethyl ether blend, which specifically indicated the formation of a 1:2 complex [Co(*L*-His)$_2$]. As shown in Figure 1, each *L*-histidine acts as a tridentate ligand with linkage via carboxylate, amine, and imidazole motifs, producing an octahedrally coordinated cobalt ion. Here, the imidazole groups are oriented in a *trans* geometry, whereas the carboxylates and amines are *cis*-coordinated. The details of the crystal structure, including the notable bond lengths and bond angles, are provided in the supporting information (Tables S1 and S2).
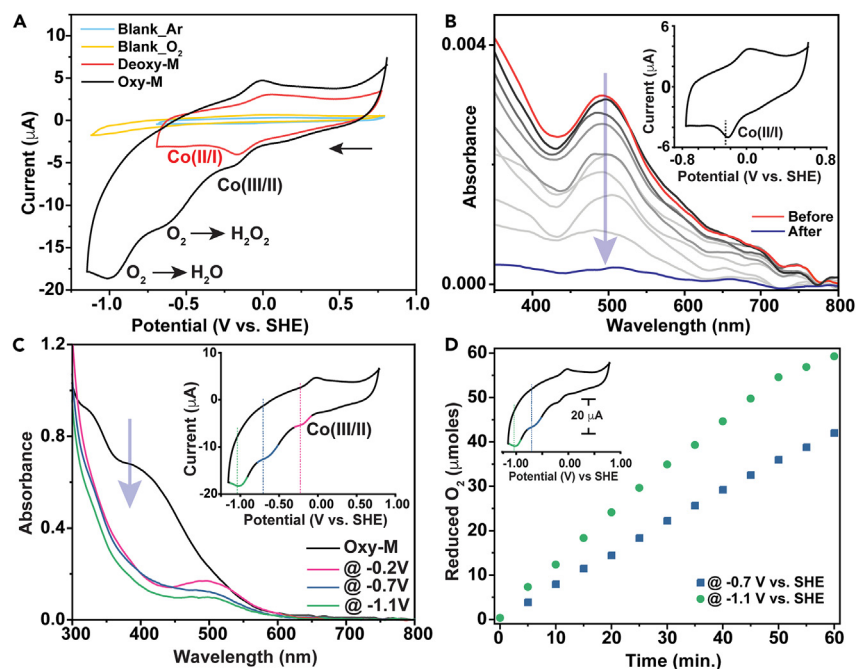
**Figure 2. The electrochemical oxygen reduction studies**

(A) Comparative cyclic voltammograms of Deoxy-M complex under 1 atm Ar (Red trace), Oxy-M complex under 1 atm $O_2$ (Black Trace), and the control blank under Ar (Sky Blue trace) and $O_2$ (Yellow trace) at pH 7. Oxy-M displays two catalytic ORR signals at 0.6 V and 0.9 V (versus SHE) along with stoichiometric Co(III/II) signal. A 1 mm glassy carbon disc electrode, a Pt wire, and Ag/AgCl in saturated KCl were used as working, counter, and reference electrodes, respectively, during this experiment. The data were recorded at 1 V s$^{-1}$ scan rate. The horizontal black arrow indicates the initial scan direction.

(B) Spectroelectrochemical studies of deoxy-M displaying a uniform decrease of the absorption profile around 500 nm, indicating a role for the redox shift of Co (II/I) during the catalytic cycle.

(C) Spectroelectrochemical studies of oxy-M showcasing a consistent decline in the absorption profile (bands at 350 and 410 nm), with the concomitant formation of 500 nm band suggesting the involvement of Co (III/II) redox change during catalytic cycle.
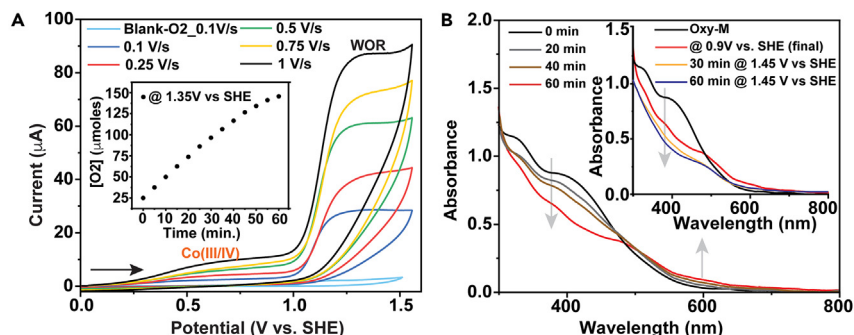
(D) Measuring the amount of oxygen reduced during bulk electrolysis at the applied potential of $-0.7$ V and $-1.1$V versus SHE in a 1.56 mM oxy-M sample in 0.1 M MES buffer solution at pH 7.0 under 1 atm $O_2$ in a closed vessel.

The exposure of this paramagnetic Deoxy-M complex (Figures S4 and S5) to $O_2$ resulted in a sharp change in the solution color with the generation of diamagnetic Oxy-M species (Figure S7). A series of complementary spectroscopic experiments validated a two-electron reduction of $O_2$ to peroxo species ($O_2^{2-}$), where two Co(II) ions share one electron each. Hence, the Oxy-M molecule showcases a binuclear *trans*-1,2-Co(III)-peroxo core, where the rapid reorientation of *L*-histidine facilitates the $O_2$ binding (Figure S2).

## Electrochemical investigation

The reversible alteration between Deoxy-M and Oxy-M in an aqueous solution indicated that this Co(*L*-His)$_2$ complex could easily activate $O_2$ via a two-electron reduction. Therefore, we decided to further probe this natural $O_2$ reducing activity of the cobalt complex in water via electrochemistry. Here, all the potential values are reported against standard hydrogen electrode (SHE) unless otherwise mentioned, which was measured with an internal standard after each experiment. The initial study was performed with a Deoxy-M sample dissolved in a buffered aqueous solution (pH 7.0) under an Ar atmosphere. During this study, a distinct reversible signal centered around $-0.2$ V was observed during a reductive scan ranging from 0.75 to $-0.75$ V (Figures 2A and S8A). The current response of this signal varies linearly with √(scan rate) to illustrate the stoichiometric nature of this signal (Figure S8B). Next, a complementary spectroelectrochemical measurement was conducted to decipher the origin of this reversible feature. Here, a chronocoulometric experiment was performed at $-0.23$, ensuring the complete reduction of the Deoxy-M sample beyond the stoichiometric signal. The gradual change of the sample was monitored in tandem with an optical spectroscopic setup that exhibited a uniform decrease of the Co(II)-centric absorption band near 500 nm (Figure 2B). Hence, this experiment validated the presence of a stoichiometric Co(II/I) reduction process.

Next, the same Deoxy-M solution was saturated with molecular oxygen with controlled purging to produce the Oxy-M sample *in situ*. The cyclic voltammogram of this sample displayed three reductive features during a reductive scan spanning from 0.75 V to $-1.25$ V (Figures 2A and S9). Initially, a reversible electrochemical signal was noticed at $-0.25$ V, whose linear variation with √(scan rate) indicates the presence of a possible stoichiometric redox step here (Figure S10). The strong LMCT bands attributed to *trans*-μ-1,2-Co(III)-peroxo core present in the Oxy-M sample gradually disappeared along with the emergence of a Co(II)-centric 500 nm band when a spectroelectrochemical experiment

**Figure 3. The electrochemical oxygen evolution studies**

(A) Cyclic voltammograms acquired at different scan rates for 0.1 mM Oxy-M in an aqueous buffered solution (pH = 7). The inset figure depicts the amount of oxygen produced during bulk electrolysis at 1.45 V versus SHE in a 1.56 mM oxy-M solution in a closed vessel. All the CVs were recorded with a 1 mm diameter glassy carbon disc working electrode, Pt wire counter electrode, and Ag/AgCl (in saturated AgCl) reference electrode in the presence of a 0.1 M $Na_2SO_4$ electrolyte. The horizontal arrows denote the initial scan direction.

(B) Spectroelectrochemical measurements of oxy-M at 0.9 V versus SHE revealing a consistent increase in the absorption profile around 610 nm indicate that the redox shift of Co (III/IV) plays a part in the catalytic cycle. Inset shows the spectroelectrochemical investigations of oxy-M at 1.45 V versus SHE demonstrating a shift in the absorption profile (bands at 550 and 610 nm) during the catalytic cycle are depicted in the figure inset.

was executed at this feature (Figure 2C). Thus, this first reversible reduction signal was attributed to Co(III/II) reduction. Two irreversible reductive peaks followed next, centered around −0.6 and −0.9 V, respectively (Figure 2C). The current responses of both these signals plateaued at elevated scan rates displaying their catalytic nature (Figures S11 and S12). The corresponding spectroelectrochemical data demonstrated the continued presence of the Co(II) feature with a slight drop in the corresponding absorbance to showcase the key role of Co(II) species in catalysis (Figures 2C and S14–S16).

As these reductive catalytic signatures appeared only in molecular oxygen, they are possibly linked with electrocatalytic oxygen reduction reactions (ORR). As mentioned earlier, the Oxy-M species contain a peroxo motif, which can be extracted as $H_2O_2$ with the addition of a proton source.[51] Hence, we have attempted to rationally probe the two electrocatalytic oxygen reduction reactions. Here, two-electron reduction to $H_2O_2$ and four-electron reduction to $H_2O$ emerge as the possible fate of the electrocatalytic ORR observed here.

$$O_2 + 2H^+ + 2e^- \rightleftharpoons H_2O_2 \qquad \text{(Equation 1)}$$

$$O_2 + 4H^+ + 4e^- \rightleftharpoons 2H_2O \qquad \text{(Equation 2)}$$

Next, bulk electrolysis (chronocoulometric) experiments were performed at both the catalytic features (−0.7 and −1.1 V) with Oxy-M sample in an oxygen-saturated aqueous solution to further validate the course of electrocatalytic ORR. This experiment was executed in an air-tight electrochemical cell fitted with a fluorometric oxygen sensor to probe the change in oxygen concentration during the experiment. During this experiment, a gradual drop in $O_2$ concentration was noticed along with a constantly increasing reductive current (Figures 2D and S17). Interestingly, the consumption of $O_2$ and amplitude of reductive current were higher at −1.1 V compared with −0.7 V experiment. The signature ORR signal currents vary significantly with an altered $O_2$ concentration (Figure S20). A concomitant drop in the $O_2$ level was also detected at both the potentials in the electrochemical cell headspace (Figures 2D and S21). A complementary rotating ring disc electrode (RRDE) experiment was carried out during the oxygen reduction process to investigate the potential formation of partially reduced peroxide species (Figure S22). In this experiment, a glassy carbon disc-Pt ring RRDE setup was utilized. The Pt ring electrode was held at a constant potential of 0.8 V, where it can oxidize the *in situ* generated $H_2O_2$ and provide us a quantitative measurement of the two-electron ORR process. We observed that 91.25% of $H_2O_2$ was produced when the applied potential in the glassy carbon disc electrode was −0.7 V. The formation of ~92% $H_2O_2$ around the first reduction peak was corroborated further with the xylenol orange assay following a chronocoulometric experiment performed at −0.7 V.[48,52] Interestingly, the $H_2O_2$ concentration reduced significantly to 11% as the glassy carbon disc electrode potential was shifted to further cathodic zone (−1.1 V) (Supporting information). The drop in the H2O2 production during the second reduction wave was also noticed in the complementary RRDE experiment (Figure S23). These data indicated that the major product of the first reduction process is $H_2O_2$ (via a two-electron reduction process, Equation 1). On the other hand, the electrocatalytic reduction at −1.1 V primarily proceeds through a complete four-electron ORR to water (Equation 2). Field emission scanning electron microscopy coupled with energy-dispersive X-ray spectroscopy (FE-SEM/EDS) was used to investigate the plastic chip working electrode used in the bulk electrolysis experiment. These data showed that the complexes were stable under electrocatalytic ORR conditions by the absence of cobalt deposition on the electrode material (Figure S18).

The electrochemical behavior of oxy-M in the oxidation direction was also investigated in a buffered aqueous solution (pH 7) under 1 atm of $O_2$. The oxidation scan revealed two irreversible signals during an anodic run ranging from 0 V to 1.55 V (Figure 3A). The first irreversible wave was observed at 0.75 V. To assign the redox couple associated with this wave, an auxiliary spectroelectrochemical measurement was

**Table 1. The electrocatalytic and photocatalytic ORR/OER parameters recorded for Oxy-M**

| Parameters | ORR | | OER |
|---|---|---|---|
| Measured electrocatalytic parameters for Oxy-M[a] | | | |
| TOF ($k_{obs}$, s$^{-1}$) | @−0.7V | @−1.1V | 15606 ($\pm$100) |
| | 250 ($\pm$5) | 66 ($\pm$2) | |
| OP (η, V) | 0.6 ($\pm$0.01) | 1.55 ($\pm$0.01) | 0.29 ($\pm$0.01) |
| Measured Photochemical Parameters for Oxy-M[a] | | | |
| TON (versus Catalyst) | 249 | | 540 |

[a]The standard deviations were calculated from a replicate of three studies.

performed. It is interesting to note that the signature LMCT band of Oxy-M sample's trans—1,2-Co(III)-peroxo core eventually faded during this oxidation with the simultaneous appearance of a new band around 625 nm (Figure 3B). A similar peak was noticed earlier during an analogous irreversible anodic electrochemical process related to cobalt(IV)-oxo species generation.[39] Hence, this first oxidation signal is attributed to Co(III)/Co(IV)-O redox change.[53] Upon further scanning toward more positive potential, the second oxidative peak at 1.35 V was observed with a significant increase in the current response.

The relationship between this second oxidative signal and √scan rate confirmed its catalytic nature (Figure S25). A bulk electrolysis experiment was performed next to determine the chemical nature of this second wave. This electrolysis was performed at 1.45 V for 1 h using a 1 cm$^2$ vitreous carbon electrode as the working electrode in an air-tight cell, which exhibited a constant increase in charge accumulation during the experiment along with a stable anodic current (Figure S26). The change in the head-space atmosphere of the electrochemical cell during the bulk electrolysis was probed with a calibrated phase fluorometric oxygen sensor, where a continuous growth of $O_2$ was noticed over the course of the experiment (Figure 3A, inset). The evolution of $O_2$ during this anodic oxidation at 1.45 V was also validated with a gas chromatography experiment following the injection of the head-space gas via an air-tight syringe (Figure S27). These findings point to the bidirectional electrocatalytic behavior of Oxy-M, which allows for the interconversion of water and dioxygen in either direction in an aqueous solution. During the bulk electrolysis experiment, the working electrode of a plastic chip was examined using field emission scanning electron microscopy in conjunction with energy-dispersive X-ray spectroscopy (FE-SEM/EDS). The absence of cobalt deposition on the electrode material indicated the robustness of the complexes under electrocatalytic OER conditions, as indicated by the data (Figure S18).

The electrocatalytic performance of Oxy-M for ORR and OER was assessed by the two traditional parameters: turnover frequency (TOF or $k_{obs}$) and overpotential (η). The calculation of $k_{obs}$ depends on the particular catalytic pathway followed during the reaction. Here, both the electrocatalytic processes are proceeding with the initial change in the oxidation state of the central cobalt ion. Hence, it can be assumed that the Oxy-M-driven catalytic process follows an $E_rC_i$ mechanism. The catalytic rate ($k_{obs}$) was calculated from the ratio of the catalytic current ($i_{cat}$) and stoichiometric current ($i_p$) demonstrated in Equation 3:

$$\frac{i_{cat}}{i_p} = \frac{1}{0.4463}\sqrt{\frac{RT}{nF\nu}}k_{obs}$$ (Equation 3)

where R, T, n, F, and ν refer to the universal gas constant, absolute temperature (in K) of the experimental condition, the number of electrons exchanged between the catalyst and electrode during the catalysis, Faraday's constant, and scan rate, respectively.

For ORR, the catalytic rate for the first reduction step (majorly producing $H_2O_2$ from $O_2$) was calculated to be 250 s$^{-1}$. On the other hand, the full four-electron oxygen reduction to water was occurring at a rate of 66 s$^{-1}$. For OER, the rate of four-electron oxidation of water to oxygen was evaluated to be 15606 s$^{-1}$.

The overpotential values (η) in aqueous solution are estimated using Equation 4:[41,54]

$$\boldsymbol{\eta} = \left[E_{O_2/H_2O_2 \text{ or } H_2O} - \left(0.0591 \times pH\right) - E_{\frac{cat}{2}}\right]V$$ (Equation 4)

Here $E_{O_2/H_2O_2}$ = 0.695V versus SHE and $E_{O_2/H_2O}$ = 1.23V versus SHE and $E_{cat/2}$ is the potential at which the half maxima of the maximum catalytic current is achieved. This equation was employed to compute the overpotential at neutral aqueous conditions (pH 7.0). As illustrated in Table 1, the overpotential values for electrocatalytic $O_2/H_2O_2$ (reduction), $O_2/H_2O$ (reduction), and $H_2O/O_2$ (oxidation) were 0.6, 1.55 V, and 0.29 V, respectively.

Next, we have attempted to unravel the possible reaction pathways leading to the bidirectional ORR/OER showcased by the Co(L-His)$_2$ complex in its respective reduced and oxidized states. The spectroscopic experiments from our previous study on this molecule have established the formation of trans-μ-1,2-Co(III)-peroxo species (Oxy-M) following the reaction between two molecules of mononuclear Deoxy-M and an $O_2$ molecule.[51] The peroxo-containing Oxy-M can liberate $H_2O_2$ following the exchange of two protons from an aqueous solution along with the production of two Co(III) centric molecules, which will spontaneously reduce to Co(II)-containing Deoxy-M, considering the applied potential favored it below −0.2 V. As shown in Scheme 1A, the first reductive feature possibly proceeds through this catalytic cycle to produce $H_2O_2$ as the major product. A spectroelectrochemical-IR experiment was devised to support the hypothesized catalytic mechanism by

**Table 2. List of the leading homogeneous OER electrocatalysts active in neutral aqueous media along with their catalytic parameters (TOF/OP)**

| Complex | Aqueous media condition | TOF ($k_{obs}$) | Overpotential ($\eta$, V) | Reference |
|---|---|---|---|---|
| CoH$^{\beta F}$CX-CO$_2$H Hangman scaffold | pH = 7 | 0.81 | 0.58 | Dogutan et al.[59] |
| Na[(L$_{1-3}$)Co$^{III}$] L: *o*-Diphenylene dicarboxamide | pH = 7 | 7.53–8.81 | 0.38 | Du et al.[42] |
| [Co$^{III}$(dpaq)(Cl)]Cl H-dpaq: 2-[bis(pyridin-2-ylmethyl)] amino-*N*-quinolin-8-yl-acetamide) | pH = 7 | 85 | 0.5 | Biswas et al.[28] |
| Cu$^{II}$(*cis*-(OH)-IndPY2) Ind: Indane, PY2:bis[2-pyridyl(ethylamine)) | pH = 7 | n.d. | 0.28 | Kafentzi et al.[60] |
| Cu$^{II}$ tetrakis(4-*N*-methylpyridyl)porphyrin | pH = 7 | 30 | 0.31 | Liu et al.[61] |
| [Ni(*meso*-L)](ClO$_4$)$_2$ L: (5,5,7,12,12,14-hexamethyl-1,4,8, 11-tetraazacyclotetradecane) | pH = 7 | n.d. | 0.17 | Zhang et al.[62] |
| Oxy-M | pH = 7 | 15,606 | 0.29 | This work |

following the fate of the distinct peroxo stretching band at 790 cm$^{-1}$ observed for Oxy-M species. As illustrated in Figure S28, the intensity of the peroxo signal in FTIR gradually disappeared when the reduction potential was held at −0.7 V. These data confirmed the cleavage of the cobalt-peroxo bond with a concomitant Co(III/II) reduction. When the same experiment was repeated at the second reduction feature ∼ −1.1 V, a new peak emerged at 815 cm$^{-1}$ following the disappearance of the peroxo stretching band at 790 cm$^{-1}$ (Figure S28). This new signal was attributed to the formation of Co(III)-OH intermediate, which can be generated following a reductive splitting of the *trans*-μ-1, 2-Co(III)-peroxo species.[55] This Co(III)-OH intermediate can produce water and Co(III) centers following protonation (Scheme 1A). Then, the Co(III) centers can follow the analogous pathway to complete the catalytic cycle. Hence, the Oxy-M species can proceed through a bifurcated catalytic pathway to produce either H$_2$O$_2$ (2e$^-$/2H$^+$ process) or water (4e$^-$/4H$^+$ process), depending on the applied potential.

Next, we probed the potential catalytic mechanism for the OER (H$_2$O/O$_2$) process (Scheme 1B). The spectroelectrochemical (optical) measurements of the sample at 0.9V displayed the appearance of a new signal ∼625 nm, indicating the generation of Co(IV)-O species (Figure 3B) (*vide supra*). This highly reactive Co(IV)-oxo intermediate presumably interacts with a water molecule next to generate the Co(II)-OOH (hydroperoxo) species following a two-electron exchange with the central metal, as observed even for transition metal-oxo-species-based water oxidation reactions.[56,57] The critical O-O bond formation step occurs along with the release of a proton (Scheme 1B). Next, the hydroperoxo species loses another proton along with the release of O$_2$ molecule. The synchronous exchange of two electrons and a water molecule during this step results in the formation of Co(II)-aquo intermediate, which readily regenerates the starting Co(III)-aquo species in the oxidizing environment. Here, the proton transfer step is critically connected with the key O-O origination step. An analogous electrocatalytic experiment was performed in D$_2$O with the identical amount of sample at neutral conditions to better understand the role of proton exchange in this step. Interestingly, the electrocatalytic OER response was reduced in D$_2$O sample (Figure S29). The corresponding calculation of catalytic rates for O$_2$ production in H$_2$O versus D$_2$O displayed a primary kinetic isotope effect of (KIE) of 2.53 (determined from $\frac{k_{obs\,(H_2O)}}{k_{obs\,(D_2O)}}$). These data supported our hypothesis, indicating the key role of proton transfer during the electrocatalytic OER.
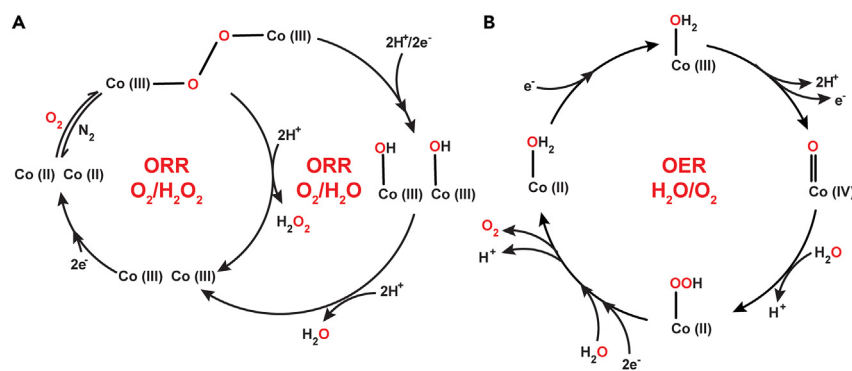


**Scheme 1. The catalytic mechanism**
(A) The possible scheme of ORR mechanism catalyzed by Deoxy-M complex followed by the addition O$_2$ under reducing conditions.
(B) The potential OER mechanism scheme followed by Deoxy-M sample during anodic oxidation of water. Here, the ligand structure is omitted in the catalytic cycles for clarity.
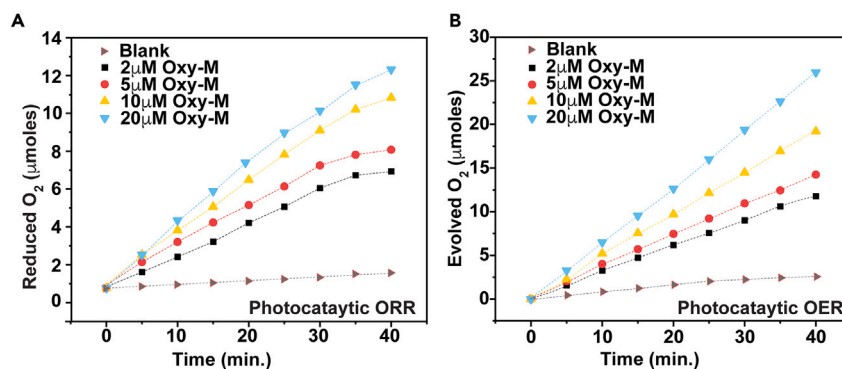
**Figure 4. The photocatalytic studies**

(A) The time trace of reduction of headspace $O_2$ level during photocatalytic ORR experiments executed in the presence of different concentrations of Oxy-M along with Eosin Y (1 mM) photosensitizer (PS) dye and sacrificial electron donor TEOA (5mM) at pH 7.0 aqueous solution.

(B) The trend of $O_2$ evolution during photocatalytic OER studies recorded for variable Oxy-M complex concentrations in the presence of Eosin Y (1 mM) photosensitizer (PS) dye and sacrificial electron acceptor $Na_2S_2O_8$ (5mM) in a neutral aqueous media (pH 7.0). All the experiments were performed with an LED irradiation $\lambda \geq 518$ nm at room temperature.

### Photocatalytic ORR and OER

The facile bidirectional electrocatalytic response displayed by the Co($L$-His)$_2$ complex in water led us to probe its reactivity even under photocatalytic conditions. Here, a photosensitizer (Eosin-Y) and an appropriate sacrificial electron donor (triethanolamine/TEOA) were deployed along with the cobalt complex present in a neutral aqueous solution during the photo-driven ORR experiment. While, a sacrificial electron acceptor ($Na_2S_2O_8$) was utilized in the place of TEOA during the photocatalytic OER, keeping the rest of the conditions the same.[36,58] During both the experiments, an LED light source ($\lambda_{max}$ 518 nm) was deployed for the photosensitization while maintaining the reaction mixture in an air-tight glass-based photochemical cell. The fluorometric oxygen sensor was utilized to monitor the alterations in the amount of oxygen in the photochemical cell headspace over the course of the experiment. During the ORR experiment, the reaction was started under a 100% $O_2$ atmosphere, where a gradual decrease in the $O_2$ concentration was noticed. This experiment was replicated in the presence of variable concentrations of Oxy-M sample. It was observed that the amount of $O_2$ mitigation increased with an increasing amount of catalyst while the rest of the conditions remained constant (Figure 4A). At lower concentrations of catalyst (2–5 μM), the photocatalytic ORR almost reached the maximum within 35 min of irradiation as showcased by the plateauing graph. The xylenol orange test was performed subsequent to the photochemical ORR investigations, wherein no discernible evidence of $H_2O_2$ production was observed. The turnover number (TON) of the photocatalytic ORR data illustrated that the maximum activity was observed for the complex at lower concentrations, as it reached a TON of 249 in the presence of 2 μM Oxy-M (Table S3).

On the other hand, the photocatalytic OER experiment was executed in an analogous air-tight glass container under 1 atm $N_2$. Here, following the irradiation, the water oxidation sets in, which was evident from the gradual $O_2$ generation, measured by the fluorometric oxygen sensor. Again, the volume of evolved $O_2$ was directly dependent on the catalyst concentration. However, the rate of $O_2$ production never dropped over 40 min of photo-irradiation at all catalyst concentrations (Figure 4B). The photocatalytic OER TON data exhibited similar trend as ORR, where the maximum TON of 540 was obtained with the lower concentration of cobalt catalyst (Table S3). The water soluble nature of the catalyst during was confirmed by complementary dynamic light scattering (DLS) experiments on before and after the photocatalysis (Figure S19). The instability of organic Eosin-Y under prolonged exposure has limited the period of the experiments, implying that the catalysts can perform better in the presence of a photo-stable photosensitizer.

The Co(L-histidine)$_2$ complex is reckoned as one of the bio-inspired models of $O_2$-carrying metalloproteins that forms a binuclear *trans*-μ-1,2-Co(III)-peroxo core following its exposure to $O_2$. Hence, this complex can readily activate $O_2$ molecules. This feature was explored further with electrochemical oxygen evolution by the complex in a neutral aqueous solution. A series of spectrochemical and electrochemical experiments were performed to validate the formation of the key *trans*-μ-1,2-Co(III)-peroxo intermediate during electrocatalytic ORR. This biomimetic complex exhibits a dual active electrocatalytic ORR, as it can preferably follow either a two-electron pathway (produces $H_2O_2$) or a four-electron process generating water. The catalyst favored the electrocatalytic $O_2/H_2O_2$ over $O_2/H_2O$, which was evident from the relatively faster rate and lower overpotential. Interestingly, we have also discovered the oxygen evolution activity of the complex under analogous conditions to establish the bidirectional ORR/OER activity by Co(L-histidine)$_2$ complex (Figure S24). This complex oxidized water to $O_2$ at an excellent rate of 15606 s$^{-1}$ with an overpotential of only 0.29 V, which is in par with the best homogeneous catalysts reported to be operational in neutral aqueous media (Table 2). The emergence of pivotal Co(IV)-oxo intermediate and involvement of kinetically significant proton exchange during the electrocatalytic OER mechanism were also validated in this study. Interestingly, this catalyst was also active under photocatalytic conditions. In the presence of Eosin-Y as a photosensitizer and appropriate redox partner, this cobalt complex can significantly reduce $O_2$ (TON 249) or oxidize water to produce $O_2$ (TON 540). Therefore, this Co(L-histidine)$_2$ complex provides us a template for designing efficient bidirectional OER/ORR catalysts that can operate even in neutral water under both electro- or photocatalytic conditions. Such catalysts will be key for unlocking the enormous potential of renewable energy resources via the small molecule activation strategy.

## Limitations of the study

This work has revealed valuable insights into the electrocatalytic and photocatalytic capabilities of the Co(L-histidine)$_2$ complex for oxygen reduction and oxygen evolution reactions. The observed catalytic activity of the complex is highly dependent on various reaction conditions, specifically on pH and temperature. Alterations in these parameters can significantly impact the catalyst's performance. Notably, the L-histidine moiety undergoes protonation at lower pH levels and deprotonation at higher pH conditions, potentially leading to the unfavourable coordination of Co in the complex. Furthermore, an increase in the temperature influences the conversion of the Co(L-histidine)$_2$ complex into the *trans*-μ-1,2-Co(III)-peroxo intermediate during electrocatalytic ORR, which significantly affects the entire catalytic cycle. Although the development of a homogeneous molecular catalyst for bidirectional O$_2$/H$_2$O transformation at neutral conditions is still in its early stages, it is worth noting that this catalyst operates at high overpotential values with mediocre turnover frequency (TOF). Hence, further investigation is required to develop the next-generation bidirectional ORR/OER catalysts that can operate in both electro- and photocatalytic conditions.

## STAR★METHODS

Detailed methods are provided in the online version of this paper and include the following:

- KEY RESOURCES TABLE
- RESOURCE AVAILABILITY
  - Lead contact
  - Materials availability
  - Data and code availability
- EXPERIMENTAL MODEL AND STUDY PARTICIPANT DETAILS
- METHOD DETAILS
  - Preparation and characterization of deoxy-M and Oxy-M
  - Single crystal X-ray diffraction study
  - Calculation of faradaic efficiency for ORR catalysis
  - Calculation of Faradaic Efficiency for WOR catalysis
  - RRDE for detection of H$_2$O$_2$
  - Xylenol orange assay for detection of H$_2$O$_2$
- QUANTIFICATION AND STATISTICAL ANALYSIS

## SUPPLEMENTAL INFORMATION

Supplemental information can be found online at https://doi.org/10.1016/j.isci.2023.108189.

## AUTHOR CONTRIBUTIONS

A.S. and A.D. conceptualize the project; A.S., C.D., and A.D. perform the experiments; A.S., C.D., S.R., D.D., A.G., P.M., and A.D. analyze the data; A.S. and A.D. wrote the manuscript; A.S., C.D., S.R., P.M., and A.D. revised and edited the manuscript; A.D. supervised the project.

## DECLARATION OF INTERESTS

There are no conflicts to declare.

## INCLUSION AND DIVERSITY

We support inclusive, diverse, and equitable conduct of research.

## REFERENCES

1. Zhang, W., Lai, W., and Cao, R. (2017). Energy-Related Small Molecule Activation Reactions: Oxygen Reduction and Hydrogen and Oxygen Evolution Reactions Catalyzed by Porphyrin- and Corrole-Based Systems. Chem. Rev. 117, 3717–3797. https://doi.org/10.1021/acs.chemrev.6b00299.

2. Pegis, M.L., Wise, C.F., Martin, D.J., and Mayer, J.M. (2018). Oxygen Reduction by Homogeneous Molecular Catalysts and Electrocatalysts. Chem. Rev. 118, 2340–2391. https://doi.org/10.1021/acs.chemrev.7b00542.

3. Lewis, N.S., and Nocera, D.G. (2006). Powering the planet: Chemical challenges in solar energy utilization. Proc. Natl. Acad. Sci. USA 103, 15729–15735. https://doi.org/10.1073/pnas.0603395103.

4. Nocera, D.G. (2012). The Artificial Leaf. Acc. Chem. Res. 45, 767–776. https://doi.org/10.1021/ar2003013.

5. Nocera, D.G. (2017). Solar Fuels and Solar Chemicals Industry. Acc. Chem. Res. 50, 616–619. https://doi.org/10.1021/acs.accounts.6b00615.

6. Seh, Z.W., Kibsgaard, J., Dickens, C.F., Chorkendorff, I., Nørskov, J.K., and Jaramillo, T.F. (2017). Combining theory and experiment in electrocatalysis: Insights into materials design. Science 355, aad4998. https://doi.org/10.1126/science.aad4998.

7. De Luna, P., Hahn, C., Higgins, D., Jaffer, S.A., Jaramillo, T.F., and Sargent, E.H. (2019). What would it take for renewably powered electrosynthesis to displace petrochemical processes? Science 364, eaav3506. https://doi.org/10.1126/science.aav3506.

8. Gayen, P., Saha, S., and Ramani, V. (2022). Pyrochlores for Advanced Oxygen Electrocatalysis. Acc. Chem. Res. 55, 2191–2200. https://doi.org/10.1021/acs.accounts.2c00049.

9. Khan, M., Janjua, N.K., Ahmad, A., Luque, R., Al-Kahtani, A.A., and Tighezza, A.M. (2022). Highly effective bi-functional electrochemical activity of Ag2O-PrO2/γ-Al2O3 electrocatalysts towards OER and ORR. Int. J. Energy Res. 46, 14161–14173. https://doi.org/10.1002/er.8133.

10. Zhang, X., Wang, X., Guan, Z., Fang, J., Sui, R., Pei, J., Qin, Y., Wei, D., Zhu, W., and Zhuang, Z. (2022). An Ultrastable Rechargeable Zinc–Air Battery Using a Janus Superwetting Air Electrode. ACS Appl. Mater. Interfaces 14, 52849–52856. https://doi.org/10.1021/acsami.2c14657.

11. Wu, Q., Ma, Y., Wang, H., Zhang, S., Huang, B., and Dai, Y. (2020). Trifunctional Electrocatalysts with High Efficiency for the Oxygen Reduction Reaction, Oxygen Evolution Reaction, and Na–O2 Battery in Heteroatom-Doped Janus Monolayer MoSSe. ACS Appl. Mater. Interfaces 12, 24066–24073. https://doi.org/10.1021/acsami.0c06062.

12. Wang, P., Lin, Y., Wan, L., and Wang, B. (2019). Construction of a Janus MnO2-NiFe Electrode via Selective Electrodeposition Strategy as a High-Performance Bifunctional Electrocatalyst for Rechargeable Zinc–Air Batteries. ACS Appl. Mater. Interfaces 11, 37701–37707. https://doi.org/10.1021/acsami.9b12232.

13. Wan, L., Wang, P., Lin, Y., and Wang, B. (2019). Janus-Typed Integrated Bifunctional Air Electrode with MnOx-NiFe LDH/Ni Foam for Rechargeable Zinc-Air Batteries.

14. J. Electrochem. Soc. 166, A3409–A3415. https://doi.org/10.1149/2.1001914jes.

15. Artero, V. (2017). Bioinspired catalytic materials for energy-relevant conversions. Nat. Energy 2, 17131–17136. https://doi.org/10.1038/nenergy.2017.131.

16. Dutta, A., Appel, A.M., and Shaw, W.J. (2018). Designing electrochemically reversible H2 oxidation and production catalysts. Nat. Rev. Chem 2, 244–252. https://doi.org/10.1038/s41570-018-0032-8.

17. Bhunia, S., Ghatak, A., Rana, A., and Dey, A. (2023). Amine Groups in the Second Sphere of Iron Porphyrins Allow for Higher and Selective 4e–/4H+ Oxygen Reduction Rates at Lower Overpotentials. J. Am. Chem. Soc. 145, 3812–3825. https://doi.org/10.1021/jacs.2c13552.

18. Awasthi, M.K., Saini, A., Das, C., Banerjee, A., Shah, N.A., Lahiri, G.K., and Dutta, A. (2023). Bio-inspired Design of Bidirectional Oxygen Reduction and Oxygen Evolution Reaction Molecular Electrocatalysts. Eur. J. Inorg. Chem. 26, e202300204. https://doi.org/10.1002/ejic.202300204.

19. Cook, E.N., and Machan, C.W. (2022). Homogeneous catalysis of dioxygen reduction by molecular Mn complexes. Chem. Commun. 58, 11746–11761. https://doi.org/10.1039/D2CC04628H.

20. Cook, E.N., Hooe, S.L., Dickie, D.A., and Machan, C.W. (2022). Homogeneous Catalytic Reduction of O2 to H2O by a Terpyridine-Based FeN3O Complex. Inorg. Chem. 61, 8387–8392. https://doi.org/10.1021/acs.inorgchem.2c00524.

21. Zhao, Y., Adiyeri Saseendran, D.P., Huang, C., Triana, C.A., Marks, W.R., Chen, H., Zhao, H., and Patzke, G.R. (2023). Oxygen Evolution/Reduction Reaction Catalysts: From In Situ Monitoring and Reaction Mechanisms to Rational Design. Chem. Rev. 123, 6257–6358. https://doi.org/10.1021/acs.chemrev.2c00515.

22. Muñoz-Becerra, K., Zagal, J.H., Venegas, R., and Recio, F.J. (2022). Strategies to improve the catalytic activity and stability of bioinspired Cu molecular catalysts for the ORR. Curr. Opin. Electrochem. 35, 101035. https://doi.org/10.1016/j.coelec.2022.101035.

23. Ginovska-Pangovska, B., Dutta, A., Reback, M.L., Linehan, J.C., and Shaw, W.J. (2014). Beyond the Active Site: The Impact of the Outer Coordination Sphere on Electrocatalysts for Hydrogen Production and Oxidation. Acc. Chem. Res. 47, 2621–2630. https://doi.org/10.1021/ar5001742.

24. Holm, R.H., Kennepohl, P., and Solomon, E.I. (1996). Structural and Functional Aspects of Metal Sites in Biology. Chem. Rev. 96, 2239–2314. https://doi.org/10.1021/cr9500390.

25. Galstyan, A., Robertazzi, A., and Knapp, E.W. (2012). Oxygen-Evolving Mn Cluster in Photosystem II: The Protonation Pattern and Oxidation State in the High-Resolution Crystal Structure. J. Am. Chem. Soc. 134, 7442–7449. https://doi.org/10.1021/ja300205n.

26. Umena, Y., Kawakami, K., Shen, J.-R., and Kamiya, N. (2011). Crystal structure of oxygen-evolving photosystem II at a resolution of 1.9 Å. Nature 473, 55–60. https://doi.org/10.1038/nature09913.

27. Dey, S., Mondal, B., and Dey, A. (2014). An acetate bound cobalt oxide catalyst for water oxidation: role of monovalent anions and

28. cations in lowering overpotential. Phys. Chem. Chem. Phys. 16, 12221–12227. https://doi.org/10.1039/C4CP01205D.

29. Ullman, A.M., Brodsky, C.N., Li, N., Zheng, S.-L., and Nocera, D.G. (2016). Probing Edge Site Reactivity of Oxidic Cobalt Water Oxidation Catalysts. J. Am. Chem. Soc. 138, 4229–4236. https://doi.org/10.1021/jacs.6b00762.

30. Biswas, S., Bose, S., Debgupta, J., Das, P., and Biswas, A.N. (2020). Redox-active ligand assisted electrocatalytic water oxidation by a mononuclear cobalt complex. Dalton Trans. 49, 7155–7165. https://doi.org/10.1039/D0DT00838A.

31. Wu, Q., Xiao, M., Wang, W., and Cui, C. (2019). In Situ Coordination Environment Tuning of Cobalt Sites for Efficient Water Oxidation. ACS Catal. 9, 11734–11742. https://doi.org/10.1021/acscatal.9b03762.

32. Wang, D., and Groves, J.T. (2013). Efficient water oxidation catalyzed by homogeneous cationic cobalt porphyrins with critical roles for the buffer base. Proc. Natl. Acad. Sci. USA 110, 15579–15584. https://doi.org/10.1073/pnas.1315383110.

33. Nakazono, T., Parent, A.R., and Sakai, K. (2013). Cobalt porphyrins as homogeneous catalysts for water oxidation. Chem. Commun. 49, 6325–6327. https://doi.org/10.1039/C3CC43031F.

34. Artero, V., Chavarot-Kerlidou, M., and Fontecave, M. (2011). Splitting Water with Cobalt. Angew. Chem. Int. Ed. 50, 7238–7266. https://doi.org/10.1002/anie.201007987.

35. Gerken, J.B., McAlpin, J.G., Chen, J.Y.C., Rigsby, M.L., Casey, W.H., Britt, R.D., and Stahl, S.S. (2011). Electrochemical Water Oxidation with Cobalt-Based Electrocatalysts from pH 0–14: The Thermodynamic Basis for Catalyst Structure, Stability, and Activity. J. Am. Chem. Soc. 133, 14431–14442. https://doi.org/10.1021/ja205647m.

36. Khosrowabadi Kotyk, J.F., Hanna, C.M., Combs, R.L., Ziller, J.W., and Yang, J.Y. (2018). Intramolecular hydrogen-bonding in a cobalt aqua complex and electrochemical water oxidation activity. Chem. Sci. 9, 2750–2755. https://doi.org/10.1039/C7SC04960A.

37. McCool, N.S., Robinson, D.M., Sheats, J.E., and Dismukes, G.C. (2011). A Co4O4 "Cubane" Water Oxidation Catalyst Inspired by Photosynthesis. J. Am. Chem. Soc. 133, 11446–11449. https://doi.org/10.1021/ja203877y.

38. Berardi, S., La Ganga, G., Natali, M., Bazzan, I., Puntoriero, F., Sartorel, A., Scandola, F., Campagna, S., and Bonchio, M. (2012). Photocatalytic Water Oxidation: Tuning Light-Induced Electron Transfer by Molecular Co4O4 Cores. J. Am. Chem. Soc. 134, 11104–11107. https://doi.org/10.1021/ja303951z.

39. Zhou, T., Wang, D., Chun-Kiat Goh, S., Hong, J., Han, J., Mao, J., and Xu, R. (2015). Bio-inspired organic cobalt(ii) phosphonates toward water oxidation. Energy Environ. Sci. 8, 526–534. https://doi.org/10.1039/C4EE03234A.

40. McEvoy, J.P., and Brudvig, G.W. (2006). Water-Splitting Chemistry of Photosystem II. Chem. Rev. 106, 4455–4483. https://doi.org/10.1021/cr0204294.

41. Das, D., Pattanayak, S., Singh, K.K., Garai, B., and Sen Gupta, S. (2016). Electrocatalytic water oxidation by a molecular cobalt complex through a high valent cobalt oxo

intermediate. Chem. Commun. *52*, 11787–11790. https://doi.org/10.1039/C6CC05773J.

40. Pegis, M.L., McKeown, B.A., Kumar, N., Lang, K., Wasylenko, D.J., Zhang, X.P., Raugei, S., and Mayer, J.M. (2016). Homogenous Electrocatalytic Oxygen Reduction Rates Correlate with Reaction Overpotential in Acidic Organic Solutions. ACS Cent. Sci. *2*, 850–856. https://doi.org/10.1021/acscentsci.6b00261.

41. Dey, S., Mondal, B., Chatterjee, S., Rana, A., Amanullah, S., and Dey, A. (2017). Molecular electrocatalysts for the oxygen reduction reaction. Nat. Rev. Chem *1*, 0098. https://doi.org/10.1038/s41570-017-0098.

42. Du, H.-Y., Chen, S.-C., Su, X.-J., Jiao, L., and Zhang, M.-T. (2018). Redox-Active Ligand Assisted Multielectron Catalysis: A Case of CoIII Complex as Water Oxidation Catalyst. J. Am. Chem. Soc. *140*, 1557–1565. https://doi.org/10.1021/jacs.8b00032.

43. Wang, Z.-Q., Tang, L.-Z., Zhang, Y.-X., Zhan, S.-Z., and Ye, J.-S. (2015). Electrochemical-driven water splitting catalyzed by a water-soluble cobalt(II) complex supported by N,N′-bis(2′-pyridinecarboxamide)-1,2-benzene with high turnover frequency. J. Power Sources *287*, 50–57. https://doi.org/10.1016/j.jpowsour.2015.04.031.

44. Zhao, Y., Lin, J., Liu, Y., Ma, B., Ding, Y., and Chen, M. (2015). Efficient light-driven water oxidation catalyzed by a mononuclear cobalt(iii) complex. Chem. Commun. *51*, 17309–17312. https://doi.org/10.1039/C5CC07448G.

45. Younus, H.A., Ahmad, N., Chughtai, A.H., Vandichel, M., Busch, M., Van Hecke, K., Yusubov, M., Song, S., and Verpoort, F. (2017). A Robust Molecular Catalyst Generated In Situ for Photo- and Electrochemical Water Oxidation. ChemSusChem *10*, 862–875. https://doi.org/10.1002/cssc.201601477.

46. Schöfberger, W., Faschinger, F., Chattopadhyay, S., Bhakta, S., Mondal, B., Elemans, J.A.A.W., Müllegger, S., Tebi, S., Koch, R., Klappenberger, F., et al. (2016). A Bifunctional Electrocatalyst for Oxygen Evolution and Oxygen Reduction Reactions in Water. Angew. Chem. *128*, 2396–2401. https://doi.org/10.1002/ange.201508404.

47. Lei, H., Liu, C., Wang, Z., Zhang, Z., Zhang, M., Chang, X., Zhang, W., and Cao, R. (2016). Noncovalent Immobilization of a Pyrene-Modified Cobalt Corrole on Carbon Supports for Enhanced Electrocatalytic Oxygen Reduction and Oxygen Evolution in Aqueous Solutions. ACS Catal. *6*, 6429–6437. https://doi.org/10.1021/acscatal.6b01579.

48. Ali, A., Prakash, D., Majumder, P., Ghosh, S., and Dutta, A. (2021). Flexible Ligand in a Molecular Cu Electrocatalyst Unfurls Bidirectional O2/H2O Conversion in Water. ACS Catal. *11*, 5934–5941. https://doi.org/10.1021/acscatal.1c01542.

49. Watters, K.L., and Wilkins, R.G. (1974). Interaction of oxygen with the cobalt(II)-histidine complex in strongly basic solution. Inorg. Chem. *13*, 752–753. https://doi.org/10.1021/ic50133a053.

50. Lever, A.B.P., and Gray, H.B. (1978). Electronic spectra of metal-dioxygen complexes. Acc. Chem. Res. *11*, 348–355. https://doi.org/10.1021/ar50129a005.

51. Saini, A., Rai, S., Maiti, D., and Dutta, A. (2022). Exploring the Cobalt–Histidine Complex for Wide-Ranging Colorimetric O2 Detection. ACS Omega *7*, 27734–27741. https://doi.org/10.1021/acsomega.2c03904.

52. Seal, M., and Dey, S.G. (2018). Active-Site Environment of Copper-Bound Human Amylin Relevant to Type 2 Diabetes. Inorg. Chem. *57*, 129–138. https://doi.org/10.1021/acs.inorgchem.7b02266.

53. Wang, B., Lee, Y.-M., Tcho, W.-Y., Tussupbayev, S., Kim, S.-T., Kim, Y., Seo, M.S., Cho, K.-B., Dede, Y., Keegan, B.C., et al. (2017). Synthesis and reactivity of a mononuclear non-haem cobalt(IV)-oxo complex. Nat. Commun. *8*, 14839. https://doi.org/10.1038/ncomms14839.

54. Roberts, J.A.S., and Bullock, R.M. (2013). Direct Determination of Equilibrium Potentials for Hydrogen Oxidation/Production by Open Circuit Potential Measurements in Acetonitrile. Inorg. Chem. *52*, 3823–3835. https://doi.org/10.1021/ic302461q.

55. Goetz, M.K., Hill, E.A., Filatov, A.S., and Anderson, J.S. (2018). Isolation of a Terminal Co(III)-Oxo Complex. J. Am. Chem. Soc. *140*, 13176–13180. https://doi.org/10.1021/jacs.8b07399.

56. Chen, Z., Concepcion, J.J., Hu, X., Yang, W., Hoertz, P.G., and Meyer, T.J. (2010). Concerted O atom–proton transfer in the O—O bond forming step in water oxidation. Proc. Natl. Acad. Sci. USA *107*, 7225–7229. https://doi.org/10.1073/pnas.1001132107.

57. Lai, W., Cao, R., Dong, G., Shaik, S., Yao, J., and Chen, H. (2012). Why Is Cobalt the Best Transition Metal in Transition-Metal Hangman Corroles for O–O Bond Formation during Water Oxidation? J. Phys. Chem. Lett. *3*, 2315–2319. https://doi.org/10.1021/jz3008535.

58. Dolui, D., Das, S., Bharti, J., Kumar, S., Kumar, P., and Dutta, A. (2020). Bio-inspired Cobalt Catalyst Enables Natural-Sunlight-Driven Hydrogen Production from Aerobic Neutral Aqueous Solution. Cell Rep. Phys. Sci. *1*, 100007. https://doi.org/10.1016/j.xcrp.2019.100007.

59. Dogutan, D.K., McGuire, R., and Nocera, D.G. (2011). Electocatalytic Water Oxidation by Cobalt(III) Hangman β-Octafluoro Corroles. J. Am. Chem. Soc. *133*, 9178–9180. https://doi.org/10.1021/ja202138m.

60. Kafentzi, M.-C., Papadakis, R., Gennarini, F., Kochem, A., Iranzo, O., Le Mest, Y., Le Poul, N., Tron, T., Faure, B., Simaan, A.J., and Réglier, M. (2018). Electrochemical Water Oxidation and Stereoselective Oxygen Atom Transfer Mediated by a Copper Complex. Chem. Eur J. *24*, 5213–5224. https://doi.org/10.1002/chem.201704613.

61. Liu, Y., Han, Y., Zhang, Z., Zhang, W., Lai, W., Wang, Y., and Cao, R. (2019). Low overpotential water oxidation at neutral pH catalyzed by a copper(ii) porphyrin. Chem. Sci. *10*, 2613–2622. https://doi.org/10.1039/C8SC04529A.

62. Zhang, M., Zhang, M.-T., Hou, C., Ke, Z.-F., and Lu, T.-B. (2014). Homogeneous Electrocatalytic Water Oxidation at Neutral pH by a Robust Macrocyclic Nickel(II) Complex. Angew. Chem. *126*, 13258–13264. https://doi.org/10.1002/ange.201406983.

# STAR★METHODS

## KEY RESOURCES TABLE

| REAGENT or RESOURCE | SOURCE | IDENTIFIER |
|---|---|---|
| Chemicals, peptides, and recombinant proteins | | |
| Co (II) chloride hexahydrate, 98% | Sigma Aldrich | SKU 255599 |
| L-Histidine, 99% | Loba Chemie | Article No. 04066 |
| Methanol | Finar chemicals Ltd. India | https://www.finarchemicals.com/product-detail/30930LC250/methanol-hplc-spectroscopy |
| Diethyl ether | Finar chemicals Ltd. India | https://www.finarchemicals.com/product-detail/30580LC100/diethyl-ether-hplc-spectroscopy |

## RESOURCE AVAILABILITY

### Lead contact

Arnab Dutta, IIT Bombay; e-mail: arnab.dutta@iitb.ac.in.

### Materials availability

The catalyst material will be provided following the request to the lead contact following the proper channel.

### Data and code availability

- Crystallographic information for complex Deoxy-M (Cambridge Crystallographic Data Centre [CCDC]: 2145265) has been provided as .cif files, and full structural factor files can be obtained at no charge from the CCDC via https://www.ccdc.cam.ac.uk/. All other data supporting the findings of this study are available within the paper and the Supplemental Experimental Procedures or are available from the authors upon reasonable request.
- This paper does not report original code.
- Any additional information required to re-analyze the data reported in this article is available from the lead contact upon request.

## EXPERIMENTAL MODEL AND STUDY PARTICIPANT DETAILS

This study does not use experimental models typical in the life sciences.

## METHOD DETAILS

### Preparation and characterization of deoxy-M and Oxy-M

The synthesis of Deoxy-M and Oxy-M form of the modelled $Co(His)_2$ complex (M). Initially two separate aqueous solutions of $CoCl_2.6H_2O$ (0.20M) and L-Histidine (0.40M) were prepared at room temperature and were completely Deoxygenated/deaerated by constant purging of argon for few minutes. The solution of L-Histidine was then added dropwise into the $CoCl_2.6H_2O$ solution under inert conditions to obtain a pink colour solution of Deoxy-M complex. Addition of dioxygen gas to this aqueous solution of Deoxy-M results in a rapid colour change to reddish brown corresponding to Oxy-M complex.

### Single crystal X-ray diffraction study

Crystals of **Deoxy-M** complex was grown by solvent diffusion method from methanol/diethyl ether. Suitable crystal was selected and mounted on a cryo-loop using cryoprotectant parafin oil. Single crystal diffraction data were collected at 100(1) K on a Bruker D8 Quest diffractometer equipped with an Incoatec Microfocus Source (IμS 3.0 Mo Kα, λ = 0.71073 Å) and a PHOTON II CCD detector. X-ray diffraction intensities were collected, integrated and scaled with APEX4 software. Empirical absorption correction was applied to the data by employing multi-scan method with SADABS programming. Structure was solved by intrinsic phasing with SHELXT and refined by full-matrix least-square methods on $F^2$ using SHELXL, using the ShelXle interface. All non-hydrogen atoms were refined with anisotropic displacement parameters. The hydrogen atoms were introduced at a calculated positions and were treated as riding atoms with an isotropic displacement parameter, C-H = 0.93-0.98 A° with Uiso(H) = 1.5 Ueq(C) for methyl groups, Uiso(H) = 1.2 Ueq(C, N) for all other C-H and N-H bonds and O-H = 0.82 A° [Uiso (H) = 1.5 Ueq(O)]. The molecular plot was drawn with Mercury 4.2. Crystal data, data collection and structure refinement details are summarized in Table S1. The crystallographic information of **Deoxy-M** (CCDC 2145265) can be obtained free of charge from the Cambridge Crystallographic Data Centre via www.ccdc.cam.ac.uk.

## EPR studies

The EPR samples were prepared, unless otherwise indicated, under inert conditions using glycerol as the solvent. Aliquots of freshly prepared Deoxy-M was transferred into Wilmad LabGlass quartz EPR tubes capped with rubber septa, and flash frozen in liquid $N_2$. The Oxy-M sample was prepared by purging $O_2$ into the Deoxy-M solution. The cw-EPR spectra was recorded using **JES - FA200 ESR Spectrometer** X-Band resonators at an average microwave frequency of 9.10 GHz.

## Nuclear magnetic resonance spectra (NMR) studies

The $^1$H-NMR experiment was performed at~300K temperature using a Bruker Avance III 500 MHz Ascent FT spectrometer with working frequencies of 500 MHz.

## Bulk or chronocoulometry experiment in aqueous buffer

Bulk Electrolysis (BE) or Chronocoulometry experiment has been carried out in an air-tight 75 mL four neck glass vessel. For ORR studies three of its neck is fitted with various electrodes; 2 cm x 1 cm vitreous carbon as working electrode; Platinum wire as counter electrode, Saturated Ag/AgCl as reference electrode. Last neck was closed by a B-14/20 suba seal rubber septum, which was used for $O_2$ purging before experiment. During experiment, 15 mL of 1.56 mM of Oxy-M was added in the vessel, all electrodes (along with a magnetic bead) were inserted along with B-14/20 rubber septum cap (in gas tight manner) and solution was purged with $O_2$ for 30 minutes. Then, purging was stopped and chrono-coulometric experiment was started at corresponding catalytic potentials (at -0.2V, at -0.7V and at -1.1V vs SHE in a pH 7 aqueous buffer solution). For WOR studies, the oxy-M solution was prepared separately and then transferred in the four nec glass vessel. All the neck were covered as stated previously. The solution was continuously stirred with a magnetic stirrer during all the experiments. The amount of oxygen reduced and evolved were measured and recorded with time by a calibrated Mettler Toledo M800 Transmitter with InPro® 6000 Optical Sensor. Blank bulk run was performed under similar condition in the absence of any catalyst.

## Calculation of faradaic efficiency for ORR catalysis

- At -0.7V
- Overall charge passed during 3600 sec ORR electrocatalysis = (9.39 - 0.67) C = 8.72C

[Blank solution charge = 0.67C]

- 2 * 96485C charge passed during ORR ($O_2 + 2H^+ + 2e^- \rightleftharpoons H_2O_2$ ) is equivalent to 1 mol of $H_2O_2$.
- Hence, 8.72 C charge passed during ORR is equivalent to (8.72/2*96485) mL = 45.18 μmoles of $H_2O_2$.
- Amount of $H_2O_2$ produced during Xylenol Orange Test after Bulk Electrolysis at -0.7V vs SHE = 41.65 μmoles.
- **Faradaic efficiency = (41.65/45.18) * 100 = 92.18%.**
- At -1.1V
- Overall charge passed during 3600 sec ORR electrocatalysis = (25.21 - 0.67) C = 24.54C [Blank solution charge = 0.67C]
- Amount of $H_2O_2$ produced during Xylenol Orange Test after Bulk Electrolysis at -1.1V vs SHE = 13.88 μmoles
- Amount of Charge accounted for $H_2O_2$ conversion = 13.88 * $10^{-6}$ * 2 * 96485 = 2.67C
- During Bulk Electrolysis the $O_2$ concentration decreased from 100% to 97.80% that is equivalent to 60 * (100-97.80)% mL = 1.32 mL of $O_2$ (head space volume = 60 mL)
- The amount of $O_2$ reduced during ORR catalysis = (1.32/22400) moles of $O_2$ = 58.92 μmoles of $O_2$
- The amount of $O_2$ consumed during $O_2 + 2H^+ + 2e^- \rightleftharpoons H_2O_2$ conversion = 13.88 μmoles of $O_2$
- The amount of $O_2$ consumed during $O_2 + 4H^+ + 4e^- \rightleftharpoons H_2O$ conversion = 58.92 – 13.88 = 45.04 μmoles of $O_2$ (or 1.008 mL of $O_2$)
- Amount of Charge accounted for $O_2$ to $H_2O$ conversion = 24.54C – 2.67C = 21.87 C
- 4 * 96485 C charge passed during ORR is equivalent to 22400 mL $O_2$. Hence, 21.87 C charge passed during ORR is equivalent to (22400 * 21.87)/(4 * 96485) mL = 1.27 mL of $O_2$
- Hence, the **Faradaic Efficiency (FE)** for $O_2 + 4H^+ + 4e^- \rightleftharpoons H_2O$ is (1.008/1.27) x 100 % = **79.37%**

## Calculation of Faradaic Efficiency for WOR catalysis

- Overall charge passed during 1-hour WOR electrocatalysis = (54.9-0.6)C = 54.3C

[Blank solution charge = 0.6C]

- 4 * 96485C charge passed during OER is equivalent to 22400 mL of $O_2$.
- Hence, 54.3 C charge passed during OER is equivalent to (22400 * 54.3)/4*96485) mL = 3.14 mL of O2
- Oxgen produced during Bulk electrolysis of complex followed by an oxygen sensor (will include the name of instrument later): 5.82% $O_2$
- Oxgen produced during Bulk electrolysis of blank solution = 0.996% $O_2$
- **Equivalents in mL =** 15 * (5.82-0.996)% mL = 2.89 mL (head-space volume = 15 mL)
- **Faradaic efficiency = (2.89/3.14) * 100 = 92.03%**

*Optical spectroelectrochemical study*

Optical spectroscopy is a vital tool for the evidence of change in metal oxidation state. For ORR three exhibited distinct peaks at -0.2 V, -0.7 V, and -1.1V vs SHE. Whereas for WOR two oxhibited distinct peaks at 0.8V and 1.45V vs. SHE. Controlled Potential Experiment (CPE) along with optical spectroscopy have been done for cathodic potentials on -0.2 V; -0.7 V; and -1.1 V vs SHE whereas for anodic potentials on 0.8V and 1.45 V vs. SHE respectively using Ocean Optics spectrophotometer on the successive interval in a pH 7 aqueous buffer solution. Optical spectra have been recorded with time to trace the changes in metal oxidation state.

*Infrared spectroelectrochemistry*

An optically transparent thin–layer electrode (OTTLE) cell, equipped with Pt mesh as working electrode, Pt microwire as counter electrode, and Ag microwire as a pseudo–reference electrode. For studies performed under $O_2$ atmosphere, the blank solutions consist of the solution of pH 7 aqueous buffer solution (0.5 M $Na_2SO_4$) under $O_2$, which later was used to subtract the solvent signals. FT–IR spectra were measured using Perkin–Elmer FT–IR spectrometer in absorbance mode. All the measurements were carried out at room temperature.

## RRDE for detection of $H_2O_2$

A Pine potentiostat was used for RRDE investigations. LSV and CV were measured in an oxygen-saturated solution with a pH of 7. The LSV of Oxy-M was done at various rotations, and the koutecky levich (K-L plot) was plotted to determine the effective number of electrons that engage in ORR, as indicated in Equation 5. The effective number of electrons transported was determined using a rotating ring disc electrode. Pt/C was employed as a comparison catalyst in both RDE and RRDE tests.

$$\frac{1}{j_m} = \frac{1}{j_k} + \frac{1}{0.62 \, nFD^{2/3} \nu^{-1/6} C} \, \omega^{-1/2} \qquad \text{(Equation 5)}$$

Where $j_m$ and $j_k$ are measured and kinetic currents, n is the number of electrons transferred,

F is faraday's constant (96485 C mol$^{-1}$), D is the diffusivity, $\nu$ is the kinematic viscosity and C is the concentration of oxygen in neutral buffered aqueous solution.

The number of electron transferred in the process were calculated using Equation 6.

$$n = \frac{4 \times I_d}{I_d + \frac{I_r}{N}} \qquad \text{(Equation 6)}$$

The % of $HO_2^-$ yield was calculated using Equation 7

$$HO_2^- \, (\%) = \frac{200 \times I_r}{(N \times I_d) + I_r} \qquad \text{(Equation 7)}$$

## Xylenol orange assay for detection of $H_2O_2$

Mohr's salt (4.9 mg) and xylenol orange (3.9 mg) were dissolved in 5 mL solution of 250 mM $H_2SO_4$ and the solution was stirred for 10 mins. In a 2mL cuvette, a 200 μL alliqout of this solution was taken, 1.8 mL of Millipore water was added to it which is marked as the reference blank, and a 250 μL portion of the solutions from bulk electrolysis performed at -0.7 V and -1.1V (vs SHE) was added separately. The UV-Vis spectrum of these solutions was recorded and a change in the 560-600 nm region was observed. For quantitative estimation of $H_2O_2$ which is a probable product of this catalytic ORR performance, a calibration curve was prepared from different solutions having 2.5 μM, 3 μM, 4 μM, 5 μM, 7 μM, 8 μM, 9 μM, 10 μM, 100 μM final concentration of $H_2O_2$ by recording their absorbance and monitoring the peak around 560-600 nm. The trend in 560-600 nm absorbance from this study were compared which suggested 41.65 μmol generation of $H_2O_2$ at -0.7V and 13.88 μmol $H_2O_2$ at -1.1V during the experiment.

## QUANTIFICATION AND STATISTICAL ANALYSIS

The measurement of catalytic rate were performed using three replicate data set and the standard deviation was calculated using Microsoft excel.